ADVANCED MATERIALS
www.advmat.de

Lightweight Electrolyte Design for Li/Sulfurized Polyacrylonitrile (SPAN) Batteries

An L. Phan, Bo Nan, Phung M. L. Le, Qiushi Miao, Zhaohui Wu, Kha Le, Fu Chen, Mark Engelhard, Thien Dan Nguyen, Kee Sung Han, Jiyun Heo, Weiran Zhang, Minsung Baek, Jijian Xu, Xiyue Zhang, Ping Liu, Lin Ma, and Chunsheng Wang**

Sulfurized polyacrylonitrile (SPAN) recently emerges as a promising cathode for high-energy lithium (Li) metal batteries owing to its high capacity, extended cycle life, and liberty from costly transition metals. As the high capacities of both Li metal and SPAN lead to relatively small electrode weights, the weight and specific energy density of Li/SPAN batteries are particularly sensitive to electrolyte weight, highlighting the importance of minimizing electrolyte density. Besides, the large volume changes of Li metal anode and SPAN cathode require inorganic-rich interphases that can guarantee intactness and protectivity throughout long cycles. This work addresses these crucial aspects with an electrolyte design where lightweight dibutyl ether (DBE) is used as a diluent for concentrated lithium bis(fluorosulfonyl)imide (LiFSI)-triethyl phosphate (TEP) solution. The designed electrolyte ($d = 1.04$ g mL^{-1}) is 40%–50% lighter than conventional localized high-concentration electrolytes (LHCEs), leading to 12%–20% extra energy density at the cell level. Besides, the use of DBE introduces substantial solvent-diluent affinity, resulting in a unique solvation structure with strengthened capability to form favorable anion-derived inorganic-rich interphases, minimize electrolyte consumption, and improve cell cyclability. The electrolyte also exhibits low volatility and offers good protection to both Li metal anode and SPAN cathode under thermal abuse.

1. Introduction

Extensive endeavors have been devoted to bridging the theory-practice gap in the energy density of lithium/sulfur (Li/S) batteries, aiming at realizing a high-energy battery technology that is free from transition metals and their associated drawbacks, such as high cost, low abundance, uneven distribution on Earth, and potential toxicity. Derived from experience with Li-ion batteries, where the energy density is primarily limited by the cathode, improving the specific capacity of S-based cathodes has always been the primary focus of such efforts.[1,2] It should be noted that Li/S batteries generally exhibit a different dynamic. In practical Li/S cells, the electrolyte tends to be the heaviest component while the electrodes account for a rather small portion of the total cell weight. This difference can be explained by the fact that Li metal anode and S-based cathodes exhibit much higher specific capacities than

A. L. Phan, J. Heo, W. Zhang, M. Baek, J. Xu, X. Zhang, L. Ma, C. Wang
Department of Chemical and Biomolecular Engineering
University of Maryland
College Park, MD 20742, USA
E-mail: l.ma@charlotte.edu; cswang@umd.edu

B. Nan, F. Chen
Department of Chemistry and Biochemistry
University of Maryland
College Park, MD 20742, USA

P. M. L. Le, K. Le
Energy & Environment Directorate
Pacific Northwest National Laboratory
Richland, WA 99354, USA

The ORCID identification number(s) for the author(s) of this article can be found under https://doi.org/10.1002/adma.202406594

DOI: 10.1002/adma.202406594

Q. Miao, Z. Wu, P. Liu
Department of Nanoengineering
University of California at San Diego
La Jolla, CA 92093, USA

M. Engelhard
Environmental Molecular Sciences Laboratory
Pacific Northwest National Laboratory
Richland, WA 99354, USA

T. Dan Nguyen, K. S. Han
Joint Center for Energy Storage Research
Pacific Northwest National Laboratory
Richland, WA 99354, USA

T. Dan Nguyen
Physical Sciences Division
Pacific Northwest National Laboratory
Richland, WA 99354, USA

L. Ma
Department of Mechanical Engineering and Engineering Science
The University of North Carolina at Charlotte
Charlotte, NC 28223, USA

those of intercalation materials.[3,4] Therefore, minimizing the electrolyte weight is a crucial prerequisite for Li/S batteries to attain high energy density. A direct consequence is that realizing high-energy Li/S cells based on the conventional solid–liquid–solid sulfur electrochemistry would be greatly challenging because of the kinetic issues and the aggravated parasitic reactions associated with the polysulfide (over)saturation in the electrolyte under lean conditions.[5,6] A straightforward solution is using sulfurized polyacrylonitrile (SPAN), a polymeric material with molecularly uniform sulfur distribution and the capability to undergo complete solid-state S conversion.[7,8] Similar to regular Li/S batteries, Li/SPAN cell-level energy density is also highly affected by the electrolyte weight, as will be discussed in detail in Section 2. Meanwhile, the electrolyte volume needs to be maintained at a certain level to ensure adequate wettability and ionic conductivity.[9,10] Lowering the electrolyte density emerges as the foremost approach.

In addition, high-energy Li/SPAN batteries also require electrolytes capable of forming inorganic-rich interphases on Li anode and SPAN cathode to accommodate their large volume changes during cycling.[11–13] Inorganic interphase components, especially LiF, have high interface energy and weak bonding to Li anode and SPAN cathode, so they suffer less stress/strain upon electrodes' volume change and can remain protective throughout long cycles. The relevance of this requirement intensifies when the SPAN capacity exceeds 600 mAh g^{-1} (note that SPAN capacity throughout this manuscript is calculated based on the SPAN mass), as this level is only achievable in the presence of weakly-bonded sulfur chains (i.e., those removable by toluene extraction[14]) known for their heightened reactivity and/or solubility in the electrolyte.[15] It should be noted that although carbonate electrolytes are known to support SPAN at low specific capacity and low electrode mass loading values (which translate into small absolute volume change), their performance with SPAN at more practical conditions is inadequate,[11,12] not to mention their notorious incompatibility with Li metal.

Localized high-concentration electrolytes (LHCEs) are currently considered one of the best choices for Li/SPAN batteries, as their special solvation structures allow the formation of anion-derived inorganic-rich interphases with good protection for both SPAN and Li metal.[6,11,13,15,16] The major shortcoming of current LHCEs in the context of Li/SPAN batteries is their reliance on hydrofluoroether diluents. The good oxidative stability of highly fluorinated diluents is optimal for high-voltage Li metal batteries, for which LHCEs were originally developed, but is not necessary for S-based systems. Meanwhile, the high fluorine content greatly raises the gravimetric density of the diluents and the electrolytes (the gravimetric density of LHCEs is generally above 1.4 g mL^{-1}). As previously mentioned and will be further demonstrated in Section 2, reducing the electrolyte density can substantially improve the opportunity for Li/SPAN batteries to simultaneously achieve high energy density and long cycle life.[17] It is worth reemphasizing that the weight and density of electrolytes only become particularly important in high-capacity systems, which explains why the high electrolyte density has never been a matter of concern in conventional Li batteries using heavy transition metal oxide cathodes.

Dialkyl ethers recently regained acknowledgment for their great benignity toward both Li metal anode and SPAN cathode.[18–21] Moreover, their stability with Li metal is supposedly superior to that of hydrofluoroethers, as it is well-known that fluorination compromises the reductive stability of solvents.[22] The intrinsically low density, weak solvating power, and high Li-compatibility of dialkyl ethers enable electrolyte formulations with concurrently low density, desirable solvation structure/interphase chemistry, and slow consumption during cycling, posing great potential for achieving new lean-electrolyte and cell-level energy density records. Nonetheless, short-chain dialkyl ethers are too volatile and shall not be considered for use at ambient conditions (e.g., the normal boiling point of diethyl ether is 35 °C). Meanwhile, electrolytes with longer-chain dialkyl ethers (i.e., only containing chains longer than C3) as the main solvent are also disqualified for use in practical Li/SPAN batteries, because they exhibit underwhelmingly low ionic conductivity (<0.6 mS cm^{-1} at room temperature with lithium bis(fluorosulfonyl)imide (LiFSI) as the salt,[23]) which, according to Wu et al.,[24] would cause severe premature Li/SPAN cell shorting, especially at relevant areal capacities (3 mAh cm^{-2} and above). From a more versatile viewpoint, however, long-chain dialkyl ethers would be perfect as a diluent (as defined by Chen et al.[25]), because their limited solvation strength fits the requirements of this role while their advantages of low density and high reductive stability are well preserved.

In this work, a novel lightweight electrolyte design, 1.7 M LiFSI in triethyl phosphate (TEP)/dibutyl ether (DBE) 1/3 v/v with a density of 1.04 g mL^{-1} (denoted as TD, **Figure 1**), is devised to demonstrate our concept. DBE is chosen because it is the most commercially available long-chain dialkyl ether and has proved compatible with Li/SPAN chemistry.[19,21] TEP is used as the main solvent (i.e., the one responsible for ion dissociation and conductivity). Remarkably, thanks to the attractive interactions between TEP and DBE, the reactivity of TEP in TD is greatly tamed, thus promoting the formation of anion-derived inorganic-rich interphases on both Li and SPAN electrodes (in comparison to TEP-based LHCEs). The robust electrochemical stability and favorable interphase chemistry of TD electrolyte facilitate a high Li plating/stripping Coulombic efficiency (Li CE) of 99.4%, which, in combination with the decent electrolyte conductivity of 1.32 mS cm^{-1} and low density of 1.04 g mL^{-1}, enables Li/SPAN batteries to achieve over 200-cycle lifespan at lean electrolyte condition of 5 g $(Ah)^{-1}$. Leaner electrolyte operation (3 g $(Ah)^{-1}$) was demonstrated in single-layer pouch-cells, showing a projected initial energy density of 205 Wh kg^{-1}. Moreover, TD offers comparable thermal stability to TT, which are among the safest known electrolytes for Li metal batteries—especially under extreme conditions,[26] while still maintaining a reasonable cost (Table S6, Supporting Information). Our work demonstrates a simple but efficient strategy to simultaneously improve the energy density and lifespan of Li/SPAN batteries while maintaining high resilience to thermal abuses. The concept of lightweight electrolyte proposed in this work might also find great prospects in optimizing the energy density for other high-capacity Li metal batteries.

2. Lightweight Electrolyte Design

Our calculations based on a reported model[4] (Discussion S1, Supporting Information) showed that for Li/S batteries under the

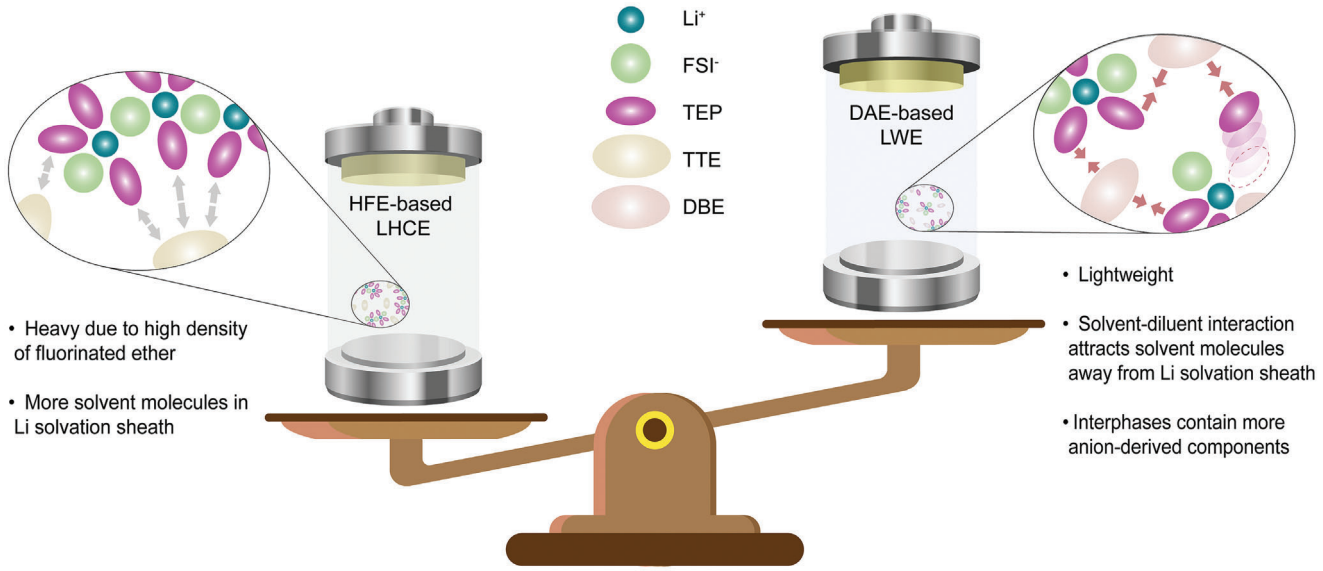

Figure 1. Demonstration of the lightweight electrolyte concept and its key merits over conventional LHCEs. HFE: hydrofluoroether; LHCE: localized high-concentration electrolyte; DAE: dialkyl ether; LWE: lightweight electrolyte.

lean electrolyte condition of 3 g_E $(Ah)^{-1}$, the electrolyte weight fraction is the highest among all cell components, given competent cathode specific capacities (above 335 mAh g^{-1}, corresponding to above 20% utilizable S content; specific capacity values are based on the total weight of the active material composite unless otherwise noted) (**Figure 2a**). This conclusion holds for the case of Li/SPAN batteries, as the SPAN capacity generally exceeds 600 mAh g^{-1}. In good agreement, Figure 2b confirms that Li/SPAN cell-level energy density is highly sensitive to the electrolyte weight, which is collectively dictated by the electrolyte density and the volume loading. The significance of reducing these two parameters becomes evident.

The use of lightweight DBE as a diluent simultaneously tackles both targets. On the one hand, it significantly diminishes the electrolyte density. For instance, the designed TD electrolyte exhibits a density of 1.04 g mL^{-1}, in contrast to 1.47 g mL^{-1} of 1.1 M LiFSI in TEP/1,1,2,2-tetrafluoroethyl 2,2,3,3-tetrafluoropropyl ether (TTE) 1/3 v/v (denoted as TT), a typical LHCE known for its great performance in Li/SPAN batteries.[15] This reduction translates into 12%–20% (or 30–40 Wh kg^{-1}) additional cell-level energy density under fixed electrolyte volume loading (Figure 2c). Conversely, when the electrolyte mass loading is fixed, TD exhibits a 40% higher volume loading than TT, resulting in delayed electrolyte depletion and enhanced cell cycle life. It should be restated that although using dialkyl ether as the sole solvent, such as in 2.0 M LiFSI in DBE[19] (denoted as 2D4), might slightly further decrease electrolyte density, the conductivity would be greatly compromised, leading to an elevated risk of Li/SPAN cell shorting.[24] On the other hand, replacing hydrofluoroether diluents with DBE limits electrolyte consumption during cycling, thereby enabling minimal electrolyte volume loading. This effect can be attributed to two factors, both rooted in the fluorine-free nature of DBE. First, DBE can interact better with the main solvent (TEP in this case). Hydrofluoroether molecules generally exhibit weak intermolecular interactions because they are covered by fluorine atoms with low polarizability.[27,28] The more robust solvent-diluent interactions help divert solvent molecules away from the Li^+ solvation sheath, mitigating their reductive decomposition on electrode surfaces and enriching interphases (cathode-electrolyte interphase (CEI) and solid-electrolyte interphase (SEI)) with favorable anion-derived components. Second, DBE is more reductively stable, a consequence of the fact that fluorination leads to lowered lowest unoccupied molecular orbital (LUMO).[22] Although TTE reductive decomposition might also supply LiF to the interphases, the potential benefits are essentially minimized by the accompanied organic by-products. Meanwhile, electrolyte dry-out has been demonstrated to be the primary factor limiting Li/SPAN battery cycle life.[17] Given that highly coordinated FSI^- anions are already present to manage the interphase chemistry, the drawback associated with TTE decomposition outweighs its advantage. The electrolyte design principle is validated by the advances in Li CE and in Li/SPAN full-cell performance at fixed limited electrolyte loading (both volume and mass), together with characterization results, as will be discussed in Sections 4 and 5.

3. Electrolyte Properties and Solvation Structure

The solvation structure of TD is derived through a comparative analysis of its spectroscopic data with other LiFSI-TEP electrolytes. **Figure 3a,b** compares the Fourier Transform Infrared (FT-IR) and Raman spectra of TD to those of a conventional LHCE (TT), a concentrated electrolyte (saturated LiFSI in TEP, denoted as sTEP), a dilute electrolyte (1.0 M LiFSI in TEP, denoted as 1TEP), the solvent (TEP), and the diluent (DBE). The diluent role of DBE is justified by the minimal shift of DBE peaks in TD compared to those of pure DBE, alongside molecular dynamics (MD) simulation results (Figure S10, Supporting Information). As expected, TD shows significant local Li^+-FSI^- interactions. FSI^--related peaks (named in black) in TD spectra are

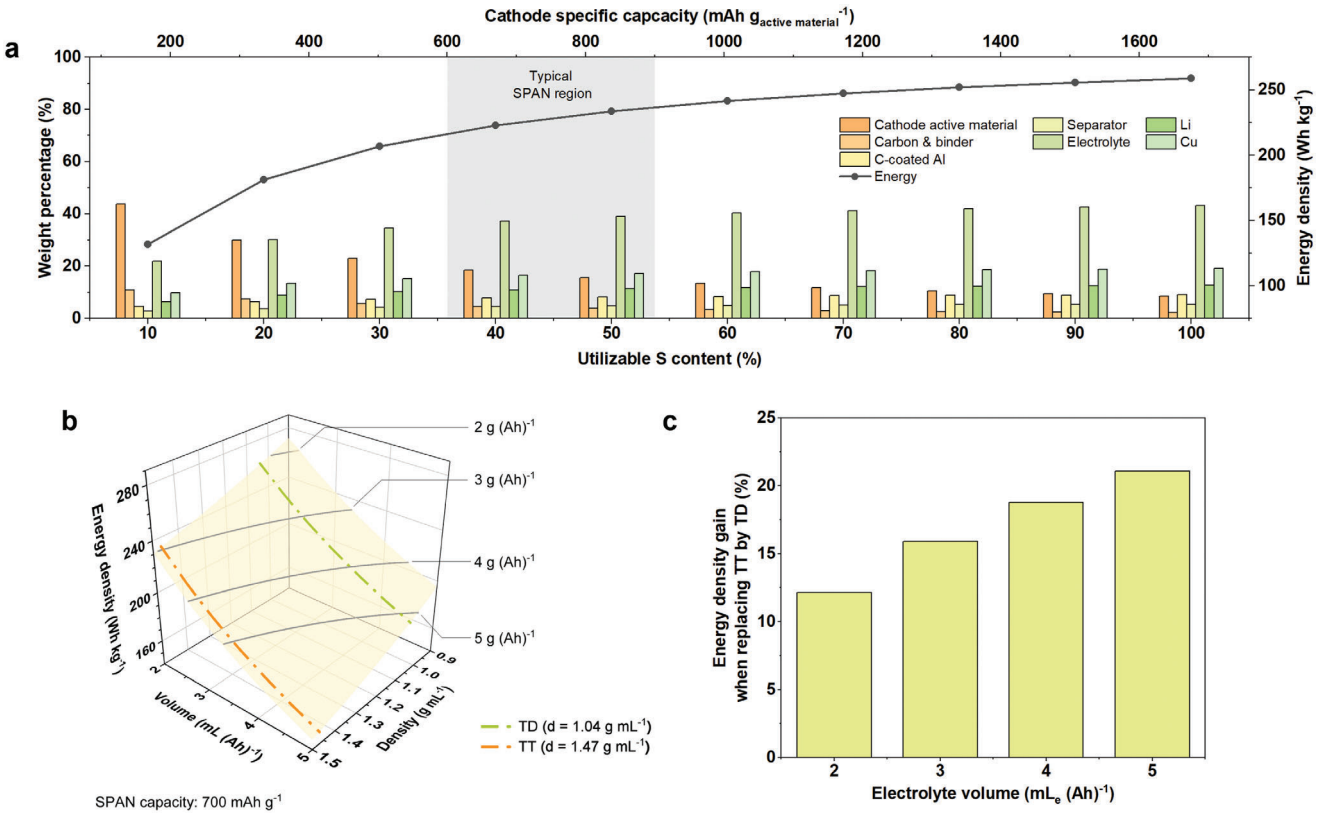

Figure 2. The motivation behind our pursuit of lightweight electrolytes for Li/SPAN batteries. a) Cell composition and energy density as functions of cathode utilizable S content and specific capacity. Data for this figure are given in Table S1 (Supporting Information). b) Impact of electrolyte density and loading on cell-level energy density. c) Improvements (in percentage) in energy density achieved when replacing TT with TD. Data for this figure are given in Table S2 (Supporting Information). For all calculations, cell active loading is 3.5 mAh cm^{-2} and negative-to-positive (N/P) ratio is 2.4. More details are shown in Discussion S1 (Supporting Information).

positioned close to those in TT and sTEP spectra, showing clear shifts from the corresponding 1TEP peaks. Furthermore, diffusivity analysis reveals that Li^+-FSI^- interactions in TD is beyond TT level. Illustrated in Figure 3c, the mobility of FSI^- in TT is notably higher than that of Li^+, indicating the presence of "free" FSI^- anions. This observation is consistent with previously reported data for TEP-based concentrated electrolytes.[29,30] In contrast, the diffusivity ratio between FSI^- and Li^+ in TD approximates one, suggesting their coordinated movement and tight binding. Meanwhile, the P═O stretching ($\nu_{P=O}$) FT-IR and Raman peaks of TD are situated close to those of 1TEP and free TEP, in contrast to TT and sTEP (Figure 3a,b). Additionally, Figure S1 (Supporting Information) shows that the already small $\nu_{P=O}$ shift of TD (relative to free TEP) is largely contributed by DBE influence. The effect of Li^+ on $\nu_{P=O}$ in TD is clearly modest compared to the cases of TT and sTEP. Since the phosphoryl oxygen is the nucleophilic and solvating site of organic phosphates, it can be inferred that TEP participation in the Li^+ solvation sheath of TD is relatively limited. ^{17}O-nuclear magnetic resonance (NMR) study (Figure S2, Supporting Information) yields similar trends: compared to the counterparts in sTEP (concentrated electrolyte) and TT (LHCE), FSI^- peaks in TD show matching shift, while $\nu_{P=O}$ peak in TD shows less deviation from free TEP. Diffusivity data (Figure 3c; and Figure S3, Supporting Information) further support our argument by showing that the relative mobility of TEP (to other electrolyte components) in TD is higher than in TT. It is well-known that solvent diffusivity tends to increase as coordination to ion-rich clusters decreases.[29,30] Finally, the fact that the activation energy for ion transport in TD (obtained by fitting the conductivity-temperature relationship into the Vogel–Fulcher–Tammann (VTF) equation, Figure 3d) better resembles that in 2D4 (weakly-solvating electrolyte) rather than that in TT (LHCE) also suggests the paucity of strong coordination between Li^+ and solvent molecules in TD. These experimental data lead us to perceive that the Li^+ solvation sheath in TD contains less TEP molecules and more FSI^- anions compared to conventional LiFSI-TEP-based concentrated electrolytes and LHCEs.

This unique feature can be attributed to the higher TEP affinity of DBE compared to that of TTE, as suggested by the smaller excess molar volume of TEP-DBE mixture compared to that of TEP-TTE mixture (Figure 3e). Our reasoning is further validated by 1) the cross-coupling peaks between TEP protons (O—CH_2, 4.5 ppm) and DBE protons (O—CH_2, 3.8 ppm and —CH_3, 1.3 ppm) observed from ^1H—^1H correlation spectroscopy (COSY) results (Figure S4, Supporting Information); and 2) the shift of (P)—O—C in phase stretching ($\nu_{(P)\text{-}O\text{-}C,ip}$) peak of TEP upon DBE addition (Figure S1, Supporting Information). In aggregate, the evidence suggests that DBE helps to attract TEP molecules away from the Li^+ solvation sheath, thus strengthening

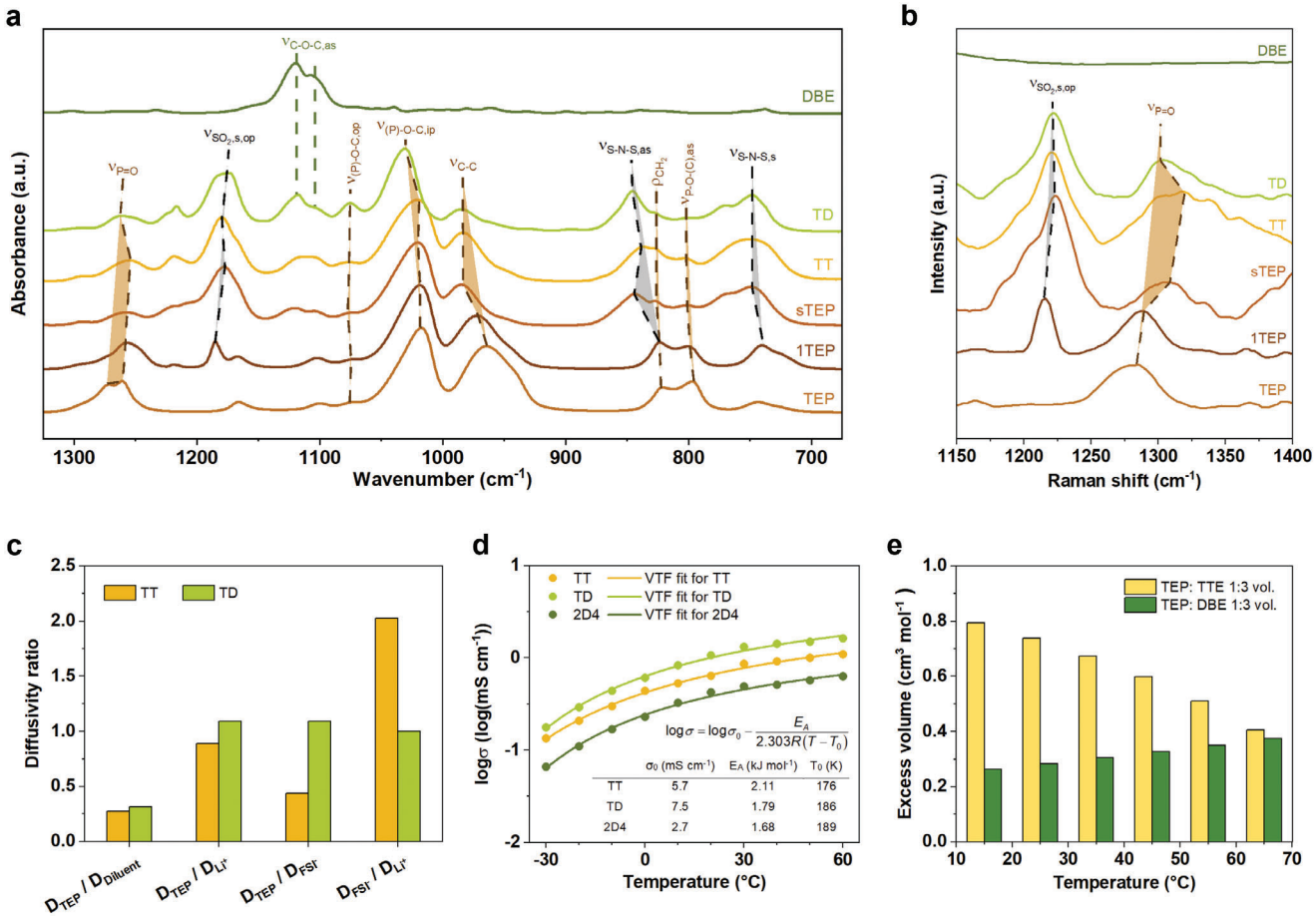

Figure 3. Characterizations of the TD solvation structure. a,b) FT-IR a) and Raman b) analyses. Peaks in brown, black, and green are from TEP, LiFSI, and DBE, respectively. c) Comparison of diffusivity ratios. Diffusivity data were collected using pulsed field gradient nuclear magnetic resonance (PFG-NMR) and are shown in Figure S3 (Supporting Information). d) Ionic conductivity from −30 to 60 °C, featuring Vogel–Fulcher–Tammann (VTF) fit results. e) Excess molar volumes (i.e., deviation from the ideal-mixing volume) of TEP/TTE and TEP/DBE mixtures.

Li^+-FSI^- coordination. This observation correlates well with the fact that TD can provide favorable interphases with less solvent-derived compositions, as will be discussed in Section 5.

Boiling point and vapor pressure also serve as important criteria to evaluate the electrolyte viability in practical battery systems.[35–37] As shown in **Figure** 4a, TEP and DBE (used in TD) show a good balance between boiling point and density. Figure 4b confirms that both TEP and DBE have lower room-temperature vapor pressure than conventional carbonate electrolytes, not to mention common thinning solvents and/or diluents. Given that carbonate electrolytes are commercially accepted in Li-ion batteries, the volatility of TD should be of no concern.

Apart from the intrinsic properties of the electrolytes, their interactions with the electrodes at elevated temperatures also have significant implications on cell robustness. Accelerating rate calorimetry (ARC) is used here to characterize the reactivity of TD with lithiated SPAN and Li metal, in comparison to that of TT and a convention carbonate electrolyte (1.0 M $LiPF_6$ in EC/EMC 3/7 w/w or Gen II), aiming to provide a qualitative evaluation of the cell safety under thermal abuses. Regarding reactivity toward lithiated SPAN (Figure 4c), all samples exhibit similar self-heating rates (SHR) up to around 180–190 °C. The sudden increase in SHR of the carbonate sample at around 200 °C, however, indicates that the conventional carbonate electrolyte might aggravate the exothermic degradation of lithiated SPAN during a self-heating scenario. Meanwhile, TD and TT clearly show less reactivity (lower SHR) toward Li metal anodes compared to the carbonate-based Gen II electrolyte (Figure 4d). In brief, TD shows thermal resilience on par with TT, surpassing that of carbonate electrolytes. It is worth highlighting that among liquid electrolytes for Li metal batteries, TEP-based LHCEs are renowned for their top-grade nonflammability.[26]

4. Electrochemical Performance of Li/SPAN Battery Using Lightweight TD Electrolyte

In general, TD electrolyte enables better cyclability of Li metal anode and Li/SPAN full-cells than TT and 2D4 reference electrolytes, especially when the electrolyte amount is limited. The Li plating/stripping process in TD entails less overpotential growth over time than that in TT and 2D4 electrolytes

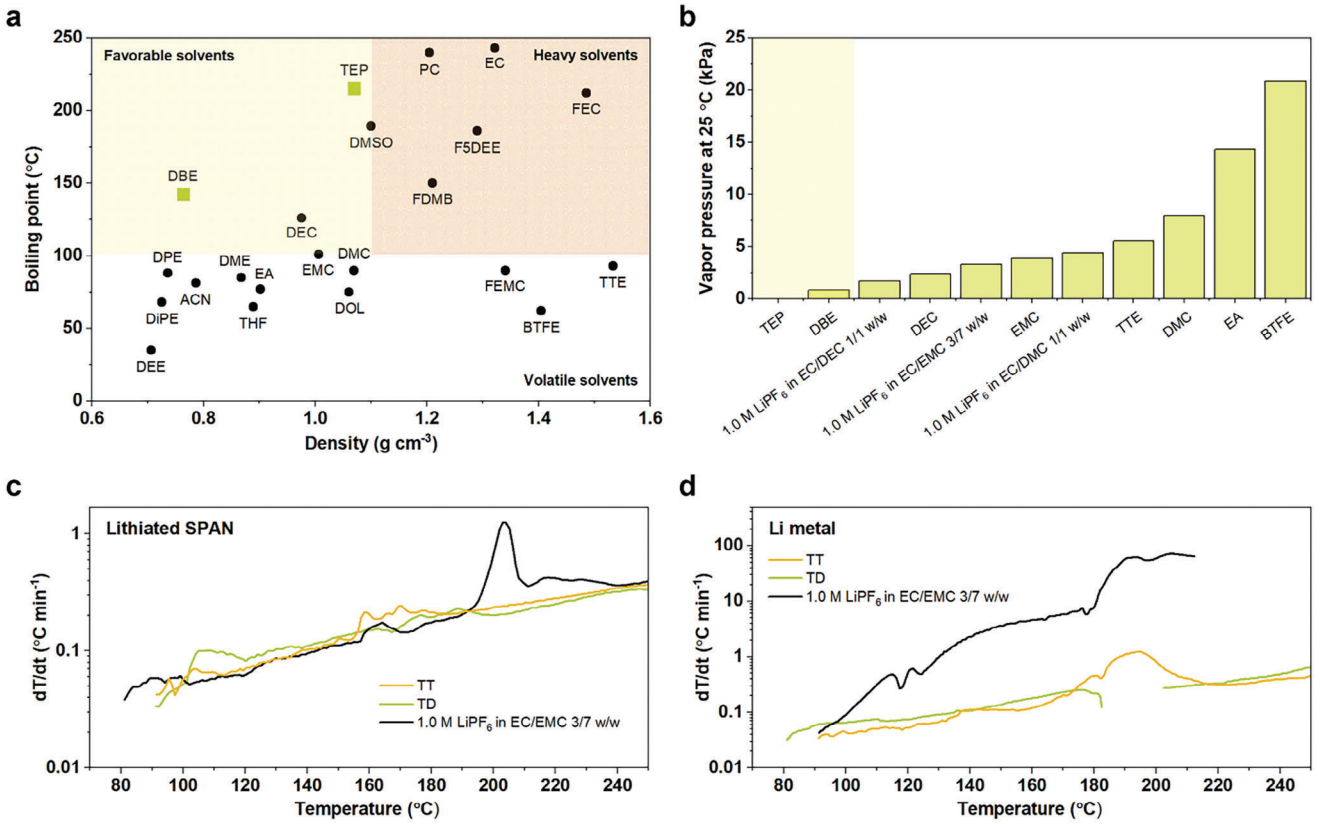

Figure 4. Analysis of electrolyte volatility and resilience toward thermal abuse. a,b) Volatility of TEP and DBE in comparison to common electrolytes/solvents for Li-based batteries: boiling point—density mapping a), and vapor pressure at 25 °C b). The vapor pressure values were adopted from literature.[31–34] c,d) Self-heating rate (SHR) of various electrolytes when coupled with lithiated SPAN cathode c) and Li metal anode d). The data were collected from accelerating rate calorimetry (ARC) experiments.

(Figure S5, Supporting Information), while offering higher average Li plating/stripping Coulombic efficiency (Li CE) of 99.4% (**Figure** 5a,b). Li/SPAN full-cells (3.5 mAh cm^{-2} SPAN, 60 µm Li, N/P = 2.4) cycled in TD also exhibit superior cyclability with 85% capacity retention after 250 cycles, compared to 69% retention after 250 cycles for TT and cell failure after around 65 cycles for 2D4, as shown in Figure 5c,d. The behavior of 2D4 (σ = 0.49 mS cm^{-1} at 30 °C) is consistent with the previous reports that electrolytes with low ionic conductivity are not suitable for high-loading Li/SPAN batteries as they promote the likelihood of a short circuit.[24] Meanwhile, the faster capacity decay in TT electrolyte can be attributed to its inferior reductive stability, as characterized by its lower Li CE (Figure 5a). Additionally, Li-SPAN full-cells cycled in TT clearly show more severe impedance growth (Figure 5d and S6, Supporting Information).

The difference between TD and TT electrolytes becomes more evident at lean electrolyte conditions (Figure 5e). At 5.0 g_E $(Ah)^{-1}$, TD supports 250-cycle lifespan of Li/SPAN cells while TT-based cells show signs of electrolyte depletion as early as 50 cycles and completely fail within 10 cycles after that. The failure mode (soft short-circuit) in TT electrolytes is likely caused by the relatively high organic and low LiF content in the interphases on both Li anode and SPAN cathode (**Figure** 6b,c; and Figure S9, Supporting Information). Such interphases tend to bond strongly to the electrodes (compared to LiF-rich interphases). During cycling, they experience similar volume changes as the electrodes (>40% for high-capacity SPAN and infinite for Li anode). The exposure to substantial stress makes the interphases prone to continuous cracking. This phenomenon constantly triggers side reactions on both electrodes and weakens their structures, leading to excessive SEI/CEI accumulation and irreversible volume changes of electrodes. On anode side, it also facilitates Li dendrite growth. As both electrodes are progressively over-swollen and the internal pressure is built-up, the risk of direct electrode contact increases. Together with the breakable interphases, a soft short-circuit results. The better cycling stability of Li/SPAN cells in TD electrolyte is partially attributed to the lower density of TD, which results in larger volume loading (given the same electrolyte weight of 5.0 g_E $(Ah)^{-1}$ for both TD and TT) and delays electrolyte loss. Cycling test in Li/SPAN pouch-cells at lean electrolyte condition of 3.0 g_E $(Ah)^{-1}$ yields consistent results (Figure 5f). The observed difference in attenuation trend compared to coin-cell data might stem from the use of a leaner electrolyte condition. As the electrolyte dry-out begins early in the cycle life, when the cell components are still resilient, a period of capacity drop manifests, rather than an abrupt short-circuit. To compare the intrinsic electrochemical properties of TD and TT electrolytes, the cycling performance of Li/SPAN cells using the same electrolyte volume loading of 4.8 mL_E $(Ah)^{-1}$ (corresponding to 5.0 g_E $(Ah)^{-1}$

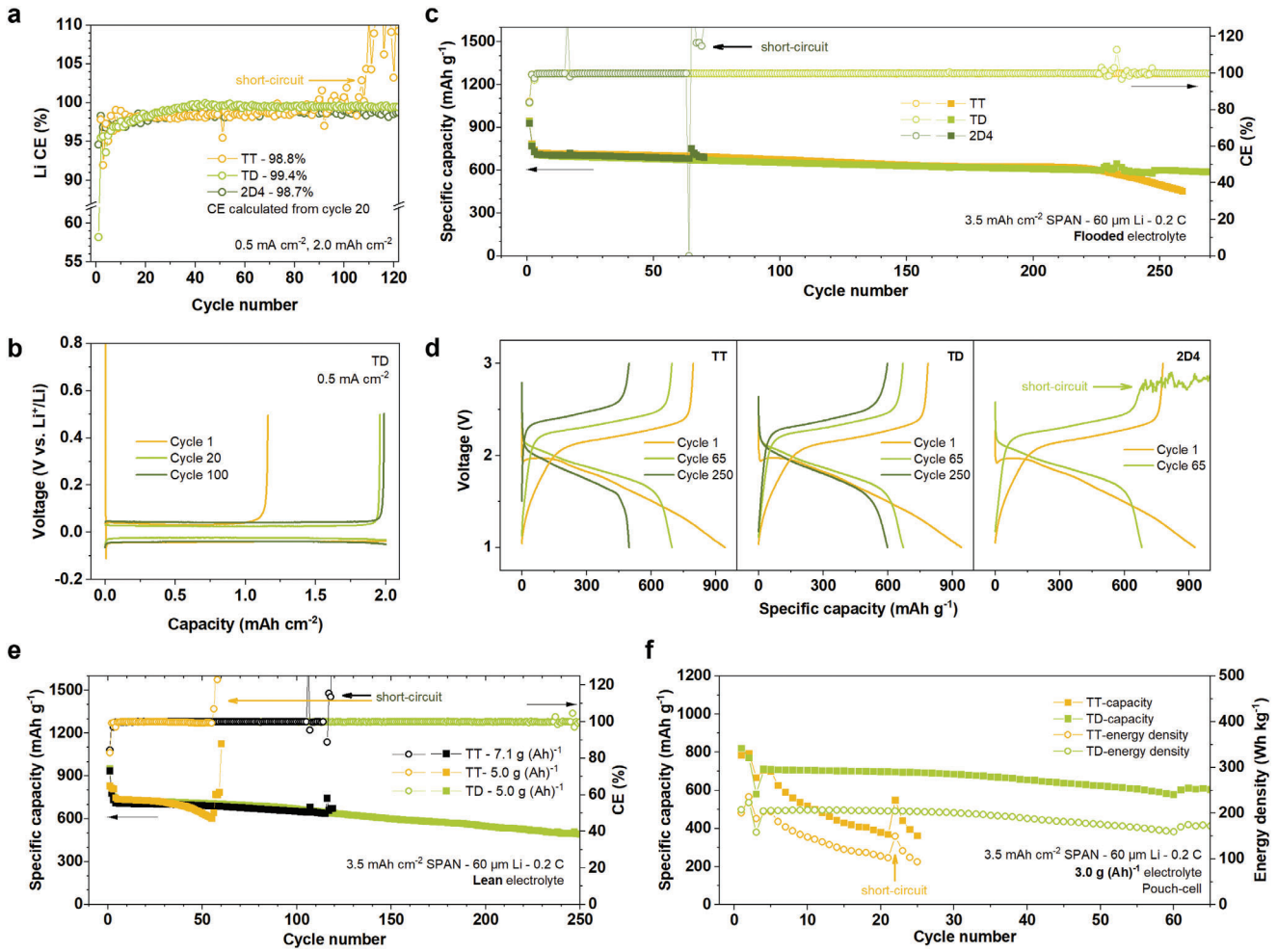

Figure 5. Electrochemical performance of the lightweight TD electrolyte. Control samples are state-of-the-art electrolytes for Li/SPAN batteries, represented by TT (LHCE) and 2D4 (weakly-solvating electrolyte). a,b) Li plating/stripping tests in Li/Cu cells: Li CE comparison a) and selected voltage profiles of the cell cycled in TD b). c,d) Li/SPAN full-cell behavior under flooded electrolyte: long-term cyclability c) and corresponding voltage profiles d). e,f) Li/SPAN full-cell behavior under lean electrolyte conditions in coin-cells e) and pouch-cells f). In coin-cell tests, an additional sample (TT −7.1 g $(Ah)^{-1}$) was included for comparison with TD at the same volume-to-capacity ratio (Note that 7.1 g $(Ah)^{-1}$ of TT and 5.0 g $(Ah)^{-1}$ of TD both correspond to a volume loading of 4.8 mL $(Ah)^{-1}$, due to their density difference).

for TD and 7.1 g_E $(Ah)^{-1}$ for TT) is also investigated. As shown in Figure 5e, TD still outperforms TT even when the effect of electrolyte density has been decoupled. This superiority can be attributed to the formation of stable inorganic-rich interphases, which effectively alleviate electrolyte consumption over extended cycling periods. Further elucidation on this matter will be presented in Section 5. In addition, our electrolyte TD also shows decent rate performance in Li/SPAN full-cells (Figure S11, Supporting Information).

5. Li Morphology, Interphase Chemistry, and Electrolyte Consumption

Post-cycling analyses were conducted on electrodes and electrolytes recovered from Li/SPAN full-cells following 50 cycles. Scanning electron microscope (SEM) images reveal a notable impact of electrolytes on plated lithium (Li) morphology (Figure 6a and S8, Supporting Information). Li cycled in TT exhibits a nodule-like shape with rounded edges/corners, along with a scattering of dendrites. Li cycled in 2D4 shows evident presence of dendrites, which aligns with the observed low electrolyte conductivity. In sharp contrast, the use of TD results in dense and flat Li deposition, characterized by relatively large (≈10 μm) and faceted particles. As recent research has found that the faceted Li morphology reflects a reduced SEI influence on Li growth dynamics,[38] it can be inferred that the SEI derived from TD is less substantial than those derived from TT and 2D4, agreeing well with the lower impedance of the cell cycled in TD (Figure S6, Supporting Information).

The SEIs derived from the three electrolytes expectedly show remarkable compositional differences (Figure 6b and S9, Supporting Information), well explaining the aforementioned divergence in Li plating/stripping behaviors. Among the samples, TT-derived SEI exhibits the lowest proportion of inorganic decomposition products, as shown in F 1s, N 1s, and S 2p X-ray photoelectron spectroscopy (XPS) spectra. Besides, its significantly higher

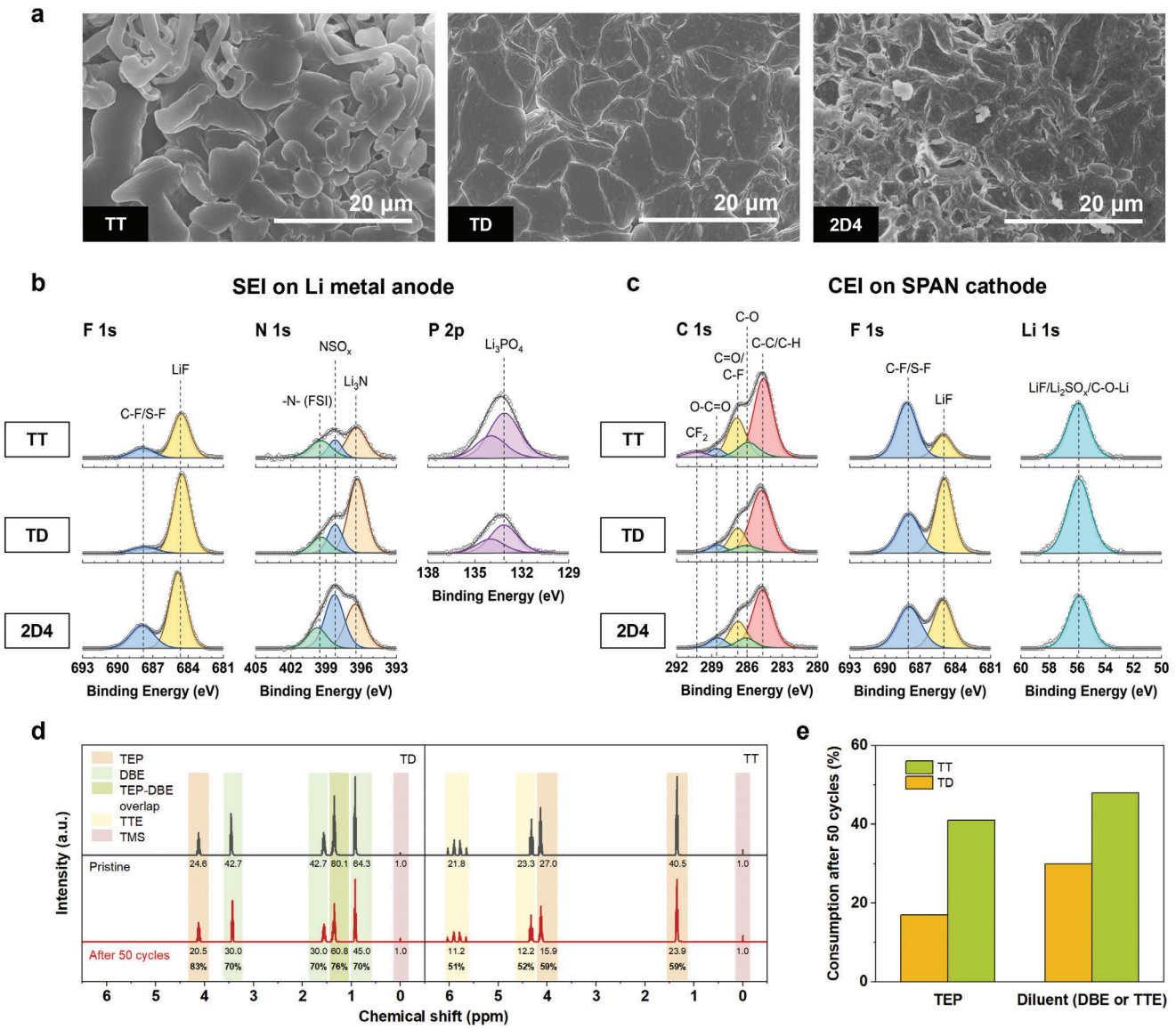

Figure 6. Analyses of electrodes and electrolytes from Li/SPAN full-cells post 50 cycles at 0.2 C. a) SEM images showing deposited Li morphology. b,c) XPS results showing the interphase composition on Li metal anode b) and SPAN cathode c). The remaining spectra are provided in Figure S9 (Supporting Information). d,e) ^{1}H-NMR analysis on the electrolyte consumption after 50 cycles: before-and-after spectra of the electrolytes d) and the quantification results e).

phosphate abundance compared to the TD counterpart indicates more contributions of solvent-derived organic compounds to the SEI, rendering the SEI more lithiophilic (i.e., having low interfacial energy toward Li metal) and promotive to dendrite formation.[39,40] In contrast, TD-derived SEI is richer in beneficial ceramic compounds, such as LiF and Li_3N. It is widely known that the low electronic conductivity of LiF and the high ionic conductivity of Li_3N, together with their good stability and high interfacial energy toward Li metal are conducive to a dendrite-free and highly reversible Li plating/stripping process.[41–44] The SEI from 2D4 contains large amounts of intermediate decomposition products from FSI^- anions, represented by S-F and NSO_x species. While these species might also be robust and lithiophobic due to their inorganic nature, they are not at their lowest redox state and thus exhibit electrochemical instability (or metastability) at low potential. In other words, they are susceptible to being further reduced and continuously changed upon long-term exposure to Li metal, which is inimical to the SEI strength. Given that subpar ion transport is the major disadvantage of 2D4 compared to TD, it might be linked to the observed lesser completeness of FSI^- reduction (for example, via causing Li^+ and/or FSI^- depletion at Li surface and encouraging solvent molecules to compete for electrons).

The same pattern was also noticed among the CEIs formed on SPAN cathodes (Figure 6c and S9, Supporting Information). Based on the LiF versus C-F/S-F (i.e., organic/metastable fluoride) ratio as well as the intensity of Li 1s peak and C 1s peaks, TD-derived CEI is the most inorganic- and LiF-rich. It is

well-known that an interphase with high LiF content shows good endurance for large electrode volume extension and is thus favorable for high-capacity materials,[45–47] including SPAN.[11,12,20] Remarkably, the presence of CF_x fragments in TT-derived interphases (both CEI and SEI) suggests the nontrivial (electro)chemical reactivity of hydrofluoroether diluents toward Li metal and lithiated SPAN, a fact that has recently garnered increasing recognition.[11,48]

Quantitative NMR data (Figure 6d,e) confirm that TD electrolyte is less consumed than TT during cycling in Li/SPAN full-cells, consistent with its enhanced cyclability under lean electrolyte conditions (Figure 5e,f). This improvement is attributable to the unique solvation structure of TD (discussed in Section 3), which not only leads to superior SEI/CEI chemistry and plated Li morphology (as revealed above by SEM and XPS analysis), but also mitigates the reducibility of TEP molecules by limiting their coordination to Li^+. The latter well explains the striking difference between TD and TT regarding TEP consumption rate. The better reductive stability of DBE, relative to TTE, might also serve as an additional contributing factor.

Overall, we have successfully demonstrated that manipulating solvent-diluent affinity to tailor the electrolyte solvation structure and interphase chemistry enhances control over the stability and/or cyclability of all cell components. Compared to TT, the conventional LHCE, better interactions between solvent (TEP) and diluent (DBE) in our TD electrolyte distract TEP away from Li^+ solvation sheath and encourage more Li^+-FSI^- coordination (as revealed from our spectroscopic analysis). More inorganic-rich SEI and CEI with better protectivity and durability against electrode volume change were obtained, effectively suppressing the unfavorable dendrite/dead Li formation, interphase thickening, and electrolyte consumption. This mechanism explains how the solvent–diluent interactions contribute to the superior cycling performance of TD electrolyte in Li/SPAN batteries under lean electrolyte conditions.

6. Conclusion

This work shows that the use of weakly-solvating dialkyl ethers, represented by DBE, as diluents results in a new electrolyte class that simultaneously satisfies the critical requirements for high-energy Li/SPAN batteries, including good electrochemical performance, decent ionic conductivity, low density, good processability (higher vapor pressure than conventional carbonates), and good safety. This combination has not been demonstrated with state-of-the-art weakly-solvating electrolytes (low conductivity) and LHCEs (high density). While the drawback of low conductivity is well documented,[24] it is worth noting that high electrolyte density can appreciably decrease the energy density of Li/SPAN (or high-capacity battery systems in general), as evidenced by around 12%–20% energy difference between cells employing our lightweight electrolyte (TD) and a conventional LHCE (TT). In addition, we found that stronger solvent–diluent attractions in TD, compared to that in TT, discourage the organic solvent molecules (in this case, TEP) from being attached to Li^+, leading to more anion-derived interphases and better overall cyclability. We believe that our work has provided a novel and comprehensive electrolyte design, bringing us closer to unlocking the full potential of Li/SPAN, as well as other Li metal batteries utilizing high-capacity cathodes.

Table 1. Electrolyte used in this study.

Name	Composition
TD	374 mg LiFSI + 267.5 mg TEP + 573 mg DBE
TT	374 mg LiFSI + 485.7 mg TEP + 2075 mg TTE
2D4	374 mg LiFSI + 764 mg DBE
sTEP	374 mg LiFSI + 485.7 mg TEP
1TEP	374 mg LiFSI + 2140 mg TEP

7. Experimental Section

Materials: LiFSI (Nippon Shokubai, 99.9%) and 1.0 M $LiPF_6$ solution in EC/EMC 3/7 w/w (Gotion) were used as received. TEP (Sigma-Aldrich, 99.8%), DBE (Sigma-Aldrich, 99.3%), and TTE (SynQuest Labs, 99%) were dried over activated molecular sieves before used. The electrolyte compositions are listed in **Table 1**. The synthesis of SPAN material and the preparation of SPAN electrodes follow a reported procedure.[24] Briefly, polyacrylonitrile (PAN, Sigma) and sulfur (325 mesh, Alfa Aesar) were mixed in 1:4 weight ratio and heated at 450 °C under Ar for 6 h to obtain SPAN powder. SPAN electrodes (on carbon coated Al foil) contain SPAN: SuperP carbon: CMC binder in 8: 1: 1 weight ratio. The active mass loading is around 5 mg_{SPAN} cm^{-2}. Li chips (500 µm thick, 12 mm diameter) were purchased from China Energy Lithium Co., Ltd. Thin Li foil coated on Cu substrate (60 µm thick) was purchased from MSE Supplies LLC. Deuterated solvents for NMR experiments, including CD_3OD (99.8% D) and CD_3Cl (99.8% D, contains 0.05 vol.% TMS) were from Cambridge Isotope Laboratories, Inc.

Electrochemical Tests: All small-scale tests were carried out in CR2032 coin-cells with one layer of Celgard separator. For Li-Cu cells, electrodeposited Cu foil of 16 mm diameter was used. The Li electrode was made of two Li chips (12 mm diameter) stacked together to ensure sufficient pressure. For Li/SPAN full cells, an additional spacer (i.e., two spacers in total, 1 mm thick each) was used for the same function, as Li thickness needed to be limited. SPAN and Li (coated on Cu) electrodes were 9 and 12 mm in diameter, respectively. For tests under flooded electrolyte condition, a fixed amount of 60 µL electrolyte was added to each coin-cell. For tests under lean electrolyte conditions, the amount of electrolyte was calculated for each coin-cell based on the corresponding active mass and electrolyte-to-capacity ratio. Large-scale tests were conducted in pouch-cells (single-layer) using rectangular 30 mm × 45 mm SPAN cathode, 35 mm × 50 mm Li (60 µm-thick, coated on Cu) anode, and one layer of Celgard 3501 separator. In an Ar-filled glovebox, dry pouch-cell was first assembled, followed by electrolyte injection (3 g $(Ah)^{-1}$) and pouch sealing under vacuum. Pouch-cells were then pressurized using stainless steel fixture before subjected to cycling tests.

Charge–discharge tests were conducted at 30 °C on CT-3008 (Neware Technology) or CT3002AU (Landt Instruments) battery testing stations. All cells were rested for 2 h before tested. Li/SPAN full-cells underwent two formation cycles at C/20 (1 C = 700 mAh g^{-1}) before long-term cycling at C/5. The voltage range was 1.0–3.0 V. All capacity values are based on the mass of SPAN. Energy density values are expressed as projected values for a multilayer pouch-cell: weights of packages, tapes, tabs are excluded; weights of current collectors are halved to represent double-sided electrodes. More details are provided in Table S5 (Supporting Information).

Electrochemical impedance spectroscopy (EIS) experiments were conducted on Gamry interface 1000E potentiostat (Gamry Instruments) from 1 MHz to 0.1 Hz using 5 mV polarization. EIS data were fitted using ZView 4 software. Ionic conductivity was measured following the reported protocol[41] with Whatman GF/A glass microfiber film as the separator and 1.0 M $LiPF_6$ in EC/DEC 1/1 v/v (Solvionic, σ = 6.3 mS cm^{-1} at 20 °C)

as the reference. The activation energy for ion transport was determined using the VTF equation as shown in Figure 3d.

Material Characterization: For SEM and XPS experiments, Li and SPAN electrodes recovered from coin-cells after 50 cycles were washed three times with DBE and dried under vacuum before tested. SEM images were collected with Hitachi SU-70 field emission scanning electron microscopy using 10 kV accelerating voltage. XPS measurements were performed using a Thermo Fisher NEXSA spectrometer with a 125 mm mean radius, full 180° hemispherical analyzer, and 128-channel detector. This system uses a focused monochromatic Al Kα X-ray (1486.7 eV) source for excitation and an electron emission angle of 60°. The narrow scan spectra were collected using a pass-energy of 50 eV with a step size of 0.1 eV. Peak fitting was performed on CASA XPS software, using Shirley background and GL(30) peak shape. For S 2p and P 2p spectra, 2p3/2 and 2p1/2 peaks were constrained to 2:1 area ratio and same fwhm; the peak separations were set to 1.18 eV for S 2p and 0.86 eV for P 2p.

For the investigation of electrolyte consumption rate, coin-cells were first prepared with 100 µL electrolyte, then dissembled immediately (for pristine samples) or after 50 cycles (for cycled samples) and washed (in whole) with 750 µL $CDCl_3$ containing 0.05 vol% TMS in a capped vial. The eluate was collected and subjected to ^{1}H-NMR quantification on a Bruker AV NEO 400 MHz instrument.

FT-IR spectra were collected with resolution of 1 cm^{-1} and scan number of 32 on a Bruker INVENIO R Spectrometer. Raman spectra were collected by a Horiba Jobin Yvon Labram Aramis spectrometer using a 532 nm diode-pumped solid-state laser. ^{17}O-NMR spectra were acquired on a Bruker AV III 600 MHz instrument (corresponding to ^{17}O frequency of 81.4 MHz) at 50 °C. Coaxial tubes were used to avoid artifacts generated by the deuterated/reference solvent (CD_3OD/CD_3Cl 1/10 v/v).

2D-NMR measurements were performed at 25 °C on a 500 MHz NMR spectrometer (Bruker, Germany) equipped with a 5-mm HX probe. For the determination of diffusion coefficients (D) of Li^+, FSI^- and solvent molecules, ^{7}Li, ^{19}F, and ^{1}H PFG-NMR were performed, respectively. The observed frequencies of ^{1}H, ^{19}F, and ^{7}Li were 500.175, 470.657, and 194.386 MHz, respectively. Each of PFG-echo profiles were obtained using a bipolar-gradient stimulated echo (stebpgp, in Topspin) sequence as a function of gradient strength (g) with the increase of g in 16 equal steps. The diffusion delay (Δ) of 100–300 ms and the gradient length (δ) of 2–4 ms were used. The number of scans was 16 for all PFG-NMR measurements. To estimate diffusion coefficient (D), the Fourier transformed echo intensity, i.e., integrated area, was fitted with the Stejskal–Tanner equation[49]

$$S(g) = S(0)\ \exp\left[-D(\gamma g\delta)^2\,(\Delta - \delta/3)\right] \quad (1)$$

where S(g) and S(0) are the echo intensities at the gradient strength of g and o, respectively; γ is the gyromagnetic ratio for the observed nucleus; $\gamma(^1\mathrm{H}) \approx 2\pi \times 42.577$ rad MHz T^{-1}, $\gamma(^{19}\mathrm{F}) \approx 2\pi \times 40.078$ rad MHz T^{-1}, and $\gamma(^7\mathrm{Li}) \approx 2\pi \times 16.546$ rad MHz T^{-1}. ^{1}H-^{1}H COSY spectra were obtained using the COSY sequence (cosygpqf, in Topspin) with the number of increments of 128 in the indirect dimension with 128 scans per increment.

Electrolyte density measurements were conducted on the Anton Paar DMA 4500 densimeter. Before each measurement, the DMA module was adjusted with a certified water standard. The system was then purged with N_2 gas to eliminate moisture and oxygen. For each measurement, 4 mL of liquid electrolyte was loaded into an air-tight syringe (vacuum-dried at 60 °C for 4 h) inside the Ar-filled glovebox (O_2 and moisture < 1 ppm). The electrolyte was subsequently injected into the DMA module at given temperatures for measurement. The temperature and density accuracy are within 0.03 °C and 0.0002 g mL^{-1}, respectively. Excess molar volumes were calculated by the following equation

$$V_m^E = \sum_i x_i M_i \left(\frac{1}{\rho} - \frac{1}{\rho_i}\right) \quad (2)$$

in which, ρ is the mixture density; ρ_i, x_i, M_i are the density, mole fraction, and molar weight of component i, respectively. Density and calculated excess molar volume data are provided in Tables S3 and S4 (Supporting Information).

Lithiated SPAN electrodes for ARC experiments were prepared by five consecutive discharges to 1.0 V with the current being halved after each discharge starting from C/10; the cells were rested for 15 min after each discharge (Figure S7, Supporting Information). Postdischarge SPAN electrodes were washed with DMC and dried under vacuum before tested. In a typical run, one SPAN electrode (1.0 mg lithiated SPAN) with 10 mg electrolyte was sealed into a stainless-steel tube with tungsten inert gas welding in the glovebox. The sample was then placed on the thermocouple within an accelerating rate calorimeter. ARC experiments were tracked under adiabatic conditions when the sample self-heating rate (SHR) was above 0.03 °C min^{-1}. As a protection protocol, experiments were set to be automatically stopped when the temperature was above 320 °C or when the SHR exceeded 10 °C min^{-1} for more than 30 s. For ARC tests with Li metal, around 5.0 mg Li and 42 mg electrolyte were used for each test. The rest of the procedure remains similar to ARC tests for lithiated SPAN.

Theoretical calculations on solvation structure were conducted by classical molecular dynamics (MD) using the Forcite module in the Material Studio 2023 software package (BIOVIA). All molecular electron densities were obtained separately from density functional theory (DFT) calculations with the DMol[3] module. All other parameters for the calculation were obtained from the COMPASSIII force field (version 1.2). For DFT calculations, electron exchange correlation was expressed using Perdew–Burke–Ernzerhof generalized gradient approximation (PBE-GGA) functional with unrestricted spin polarization, and double numerical plus polarization (DNP+) for the basis set. Convergence tolerance of energy, maximum force, and maximum displacement were set as 1×10^{-5} Ha, 2×10^{-3} Ha Å^{-1}, and 5×10^{-3} Å, respectively. Radial distribution function (RDF) calculations were conducted using the simulated scheme obtained by the following protocol. 1) Geometric optimization of randomly distributed configuration using force with 1×10^{-3} kcal mol^{-1} Å^{-1}, convergence tolerance of energy with 2×10^{-5} kcal mol^{-1}, and displacement with 1×10^{-5} Å. 2) An isothermal-isobaric ensemble simulation at standard atmosphere pressure (1.013×10^{-4} GPa) and room temperature (298 K) for 2 ns. 3) A canonical ensemble simulation at 298 K for 2 ns. 4) Another canonical ensemble simulation at 298 K for 5 ns.

Supporting Information

Supporting Information is available from the Wiley Online Library or from the author.

Acknowledgements

A.L.P. and B.N. contributed equally to this work. This work was supported by the Assistant Secretary for Energy Efficiency and Renewable Energy, Office of Vehicle Technologies of the US Department of Energy through the Advanced Battery Materials Research (BMR) Program (Battery500 Consortium Phase 2) under DOE contract No. DE-AC05-76RL01830 from the Pacific Northwest National Laboratory (PNNL). Lin Ma at UNC Charlotte acknowledges the support by the US National Science Foundation Award No. 2301719.

Conflict of Interest

The authors declare no conflict of interest.

Data Availability Statement

The data that support the findings of this study are available from the corresponding author upon reasonable request.

Keywords

high energy density, inorganic SEI, Li metal battery, lightweight electrolyte, sulfurized polyacrylonitrile

Received: May 8, 2024
Revised: June 21, 2024
Published online: July 4, 2024

[1] Y. Chen, T. Wang, H. Tian, D. Su, Q. Zhang, G. Wang, *Adv. Mater.* **2021**, *33*, 2003666.
[2] T. Liu, H. Hu, X. Ding, H. Yuan, C. Jin, J. Nai, Y. Liu, Y. Wang, Y. Wan, X. Tao, *Energy Storage Mater.* **2020**, *30*, 346.
[3] M. Hagen, P. Fanz, J. Tübke, *J. Power Sources* **2014**, *264*, 30.
[4] T. Liu, H. Li, J. Yue, J. Feng, M. Mao, X. Zhu, Y.-S. Hu, H. Li, X. Huang, L. Chen, L. Suo, *Angew. Chem., Int. Ed.* **2021**, *60*, 17547.
[5] M. Zhao, B.-Q. Li, H.-J. Peng, H. Yuan, J.-Y. Wei, J.-Q. Huang, *Angew. Chem., Int. Ed.* **2020**, *59*, 12636.
[6] Q. Miao, N. Solan, G. Hyun, J. Holoubek, P. Liu, *ACS Energy Lett.* **2023**, *8*, 4818.
[7] X. Zhao, C. Wang, Z. Li, X. Hu, A. A. Razzaq, Z. Deng, *J. Mater. Chem. A* **2021**, *9*, 19282.
[8] H. Yang, J. Chen, J. Yang, J. Wang, *Angew. Chem.* **2020**, *132*, 7374.
[9] N. B. Emerce, D. Eroglu, *J. Electrochem. Soc.* **2019**, *166*, A1490.
[10] S. S. Zhang, *Energies* **2012**, *5*, 5190.
[11] X. Zhang, P. Gao, Z. Wu, M. H. Engelhard, X. Cao, H. Jia, Y. Xu, H. Liu, C. Wang, J. Liu, J.-G. Zhang, P. Liu, W. Xu, *ACS Appl. Mater. Interfaces* **2022**, *14*, 52046.
[12] Z. Wu, S.-M. Bak, Z. Shadike, S. Yu, E. Hu, X. Xing, Y. Du, X.-Q. Yang, H. Liu, P. Liu, *ACS Appl. Mater. Interfaces* **2021**, *13*, 31733.
[13] H. Liu, J. Holoubek, H. Zhou, A. Chen, N. Chang, Z. Wu, S. Yu, Q. Yan, X. Xing, Y. Li, T. A. Pascal, P. Liu, *Mater. Today* **2021**, *42*, 17.
[14] S. Wang, B. Lu, D. Cheng, Z. Wu, S. Feng, M. Zhang, W. Li, Q. Miao, M. Patel, J. Feng, E. Hopkins, J. Zhou, S. Parab, B. Bhamwala, B. Liaw, Y. S. Meng, P. Liu, *J. Am. Chem. Soc.* **2023**, *145*, 9624.
[15] H. Yang, C. Guo, J. Chen, A. Naveed, J. Yang, Y. Nuli, J. Wang, *Angew. Chem., Int. Ed.* **2019**, *58*, 791.
[16] D. Guo, J. Wang, T. Lai, G. Henkelman, A. Manthiram, *Adv. Mater.* **2023**, *35*, 2300841.
[17] A. L. Phan, P. M. L. Le, C. Wang, *Joule* **2024**, *8*, 1601.
[18] J. Holoubek, H. Liu, Z. Wu, Y. Yin, X. Xing, G. Cai, S. Yu, H. Zhou, T. A. Pascal, Z. Chen, P. Liu, *Nat. Energy* **2021**, *6*, 303.
[19] G. Cai, J. Holoubek, M. Li, H. Gao, Y. Yin, S. Yu, H. Liu, T. A. Pascal, P. Liu, Z. Chen, *Proc. Natl. Acad. Sci. USA* **2022**, *119*, 2200392119.
[20] T. Ma, Y. Ni, D. Li, Z. Zha, S. Jin, W. Zhang, L. Jia, Q. Sun, W. Xie, Z. Tao, J. Chen, *Angew. Chem., Int. Ed.* **2023**, *62*, 202310761.
[21] J. Zhou, Y. Guo, C. Liang, L. Cao, H. Pan, J. Yang, J. Wang, *Chem. Commun.* **2018**, *54*, 5478.
[22] K. Xu, *Chem. Rev.* **2014**, *114*, 11503.
[23] Z. Li, H. Rao, R. Atwi, B. M. Sivakumar, B. Gwalani, S. Gray, K. S. Han, T. A. Everett, T. A. Ajantiwalay, V. Murugesan, N. N. Rajput, V. G. Pol, *Nat. Commun.* **2023**, *14*, 868.
[24] Z. Wu, H. Liu, J. Holoubek, C. Anderson, L. Shi, H. Khemchandani, D. Lu, D. Liu, C. Niu, J. Xiao, P. Liu, *ACS Energy Lett.* **2022**, *7*, 2701.
[25] S. Chen, J. Zheng, D. Mei, K. S. Han, M. H. Engelhard, W. Zhao, W. Xu, J. Liu, J. i.-G. Zhang, *Adv. Mater.* **2018**, *30*, 1706102.
[26] I. S. Buyuker, B. Pei, H. Zhou, X. Cao, Z. Yu, S. Liu, W. Zhang, W. Xu, J.-G. Zhang, Z. Bao, Y. Cui, C. Wang, M. S. Whittingham, *ACS Energy Lett.* **2023**, *8*, 1735.
[27] R. Berger, G. Resnati, P. Metrangolo, E. Weber, J. Hulliger, *Chem. Soc. Rev.* **2011**, *40*, 3496.
[28] C. A. Angell, *Molten Salts: From Fundamentals to Applications*, Springer, New York **2002**, pp. 305–320.
[29] K. S. Han, J. D. Bazak, Y. Chen, T. R. Graham, N. M. Washton, J. Z. Hu, V. Murugesan, K. T. Mueller, *Chem. Mater.* **2021**, *33*, 8562.
[30] Z. Zeng, V. Murugesan, K. S. Han, X. Jiang, Y. Cao, L. Xiao, X. Ai, H. Yang, J.-G. Zhang, M. L. Sushko, J. Liu, *Nat. Energy* **2018**, *3*, 674.
[31] L. Lepori, E. Matteoli, L. Bernazzani, N. Ceccanti, G. Conti, P. Gianni, V. Mollica, M. R. Tinè, *Phys. Chem. Chem. Phys.* **2000**, *2*, 4837.
[32] J. Murata, S. Yamashita, M. Akiyama, S. Katayama, T. Hiaki, A. Sekiya, *J. Chem. Eng. Data* **2002**, *47*, 911.
[33] S. Hess, M. Wohlfahrt-Mehrens, M. Wachtler, *J. Electrochem. Soc.* **2015**, *162*, A3084.
[34] A. Brozena, J. H. Buchanan, R. W. Miles Jr., B. R. Williams, M. S. Hulet, *J. Chem. Eng. Data* **2014**, *59*, 2649.
[35] Q. Wang, L. Jiang, Y. Yu, J. Sun, *Nano Energy* **2019**, *55*, 93.
[36] D. T. Vo, A. L. B. Phan, T. B. Tran, V. H. Nguyen, T. M. L. Le, A. Garg, S. Okada, P. M. L. Le, *J. Mol. Liq.* **2020**, *307*, 112982.
[37] K. T. T. Tran, L. T. M. Le, A. L. B. Phan, P. H. Tran, T. D. Vo, T. T. T. Truong, N. T. B. Nguyen, A. Garg, P. M. L. Le, M. V. Tran, *J. Mol. Liq.* **2020**, *320*, 114495.
[38] X. Yuan, B. Liu, M. Mecklenburg, Y. Li, *Nature* **2023**, *620*, 86.
[39] Y. Chen, M. Li, Y. Liu, Y. Jie, W. Li, F. Huang, X. Li, Z. He, X. Ren, Y. Chen, X. Meng, T. Cheng, M. Gu, S. Jiao, R. Cao, *Nat. Commun.* **2023**, *14*, 2655.
[40] X. Fan, X. Ji, F. Han, J. Yue, J. Chen, L. Chen, T. Deng, J. Jiang, C. Wang, *Sci. Adv.* **2018**, *4*, eaau9245.
[41] A. L. Phan, C. Jayawardana, P. M. Le, J. Zhang, B. Nan, W. Zhang, B. L. Lucht, S. Hou, C. Wang, *Adv. Funct. Mater.* **2023**, *33*, 2301177.
[42] S. Liu, J. Xia, W. Zhang, H. Wan, J. Zhang, J. Xu, J. Rao, T. Deng, S. Hou, B. Nan, C. Wang, *Angew. Chem., Int. Ed.* **2022**, *61*, 202210522.
[43] C. Yan, Y.-X. Yao, X. Chen, X.-B. Cheng, X.-Q. Zhang, J.-Q. Huang, Q. Zhang, *Angew. Chem., Int. Ed.* **2018**, *57*, 14055.
[44] J. Xu, V. Koverga, A. Phan, A.-M. Li, N. Zhang, M. Baek, C. Jayawardana, B. L. Lucht, A. T. Ngo, C. Wang, *Adv. Mater.* **2024**, *36*, 2306462.
[45] J. Chen, X. Fan, Q. Li, H. Yang, M. R. Khoshi, Y. Xu, S. Hwang, L. Chen, X. Ji, C. Yang, H. He, C. Wang, E. Garfunkel, D. Su, O. Borodin, C. Wang, *Nat. Energy* **2020**, *5*, 386.
[46] Y. Xiao, B. Han, Y. Zeng, S.-S. Chi, X. Zeng, Z. Zheng, K. Xu, Y. Deng, *Adv. Energy Mater.* **2020**, *10*, 1903937.
[47] J. Zheng, X. Fan, G. Ji, H. Wang, S. Hou, K. C. DeMella, S. R. Raghavan, J. Wang, K. Xu, C. Wang, *Nano Energy* **2018**, *50*, 431.
[48] R. May, J. C. Hestenes, N. A. Munich, L. E. Marbella, *J. Power Sources* **2023**, *553*, 232299.
[49] E. O. Stejskal, J. E. Tanner, *J. Chem. Phys.* **1965**, *42*, 288.